

The Tibetan Plateau Summer Monsoon in the CMIP5 Simulations

ANMIN DUAN

*State Key Laboratory of Numerical Modeling for Atmospheric Sciences and Geophysical Fluid Dynamics,
Institute of Atmospheric Physics, Chinese Academy of Sciences, Beijing, China*

JUN HU AND ZHIXIANG XIAO

*State Key Laboratory of Numerical Modeling for Atmospheric Sciences and Geophysical Fluid Dynamics,
Institute of Atmospheric Physics, Chinese Academy of Sciences, and University of Chinese Academy of Sciences,
Beijing, China*

(Manuscript received 21 September 2012, in final form 15 March 2013)

ABSTRACT

Temporal variability within the Tibetan Plateau summer monsoon (TPSM) is closely linked to both the East and South Asian summer monsoons over several time scales but has received much less attention than these other systems. In this study, extensive integrations under phase 5 of the Coupled Model Intercomparison Project (CMIP5) historical scenarios from 15 coupled general circulation models (CGCMs) and Atmospheric Model Intercomparison Project (AMIP) runs from eight atmospheric general circulation models (AGCMs) are used to evaluate the performance of these GCMs. Results indicate that all GCMs are able to simulate the climate mean TPSM circulation system. However, the large bias associated with precipitation intensity and patterns remains, despite the higher resolution and inclusion of the indirect effects of sulfate aerosol that have helped to improve the skill of the models to simulate the annual cycle of precipitation in both AGCMs and CGCMs. The interannual variability of the surface heat low and the Tibetan high in most of the AGCMs resembles the observation reasonably because of the prescribed forcing fields. However, only a few models were able to reproduce the observed seesaw pattern associated with the interannual variability of the TPSM and the East Asian summer monsoon (EASM). Regarding long-term trends, most models overestimated the amplitude of the tropospheric warming and the declining trend in the surface heat low between 1979 and 2005. In addition, the observed cooling trend in the upper troposphere and the decline of the Tibetan high were not reproduced by most models. Therefore, there is still significant scope for improving GCM simulations of regional climate change, especially in regions near extensive mountain ranges.

1. Introduction

The Tibetan Plateau (TP) monsoon is characterized by the remarkable seasonal alternations in wind and precipitation fields that occur over and around the plateau between winter and summer, with the most significant circulation differences in the surface pressure system (Tang et al. 1979). In winter, a surface cold high covers the TP, with a strong westerly jet above it, while in summer, the surface circulation over the plateau is replaced by a surface heat low, and the westerly jet in the midtroposphere decelerates significantly and moves to the north of the TP. In the upper troposphere, the

Tibetan high or South Asian high dominates the whole Asian monsoon region, with its center located over the southern TP. The TP summer monsoon (TPSM) is relatively independent of both the East Asian summer monsoon (EASM) and South Asian summer monsoon (SASM), although variations in the three systems are interlinked over various time scales. The TPSM reinforces the land–sea thermal contrast, which modulates the hemispheric wind belt in the midtroposphere and enhances the Tibetan high in the upper troposphere (Yeh and Gao 1979). In addition, it dominates the climate pattern and its variations over and around the TP, resulting in the wet climate of the southeastern TP and the dry climate to the northwest (Liu 1998). The TPSM is embedded in the continental monsoon system, and this helps to shape prominent monsoon circulations such as the low-level jet stream (Tang and Reiter 1984).

Corresponding author address: Anmin Duan, LASG, Institute of Atmospheric Physics, Chinese Academy of Sciences, P.O. Box 9804, Beijing 100029, China.
E-mail: amduan@lasg.iap.ac.cn

Many previous studies (e.g., Goswami 1998; Webster et al. 1998; Lambert and Boer 2001; Kang et al. 2002; Rajendran et al. 2004; Wang et al. 2004; Solomon et al. 2007) have shown that simulating monsoon systems such as the SASM and EASM, especially their variability, is one of the most challenging problems for atmospheric general circulation models (AGCMs) and coupled general circulation models (CGCMs). Annamalai et al. (2007) analyzed monsoon simulations over the twentieth century from 18 CGCMs in the Intergovernmental Panel on Climate Change (IPCC) Fourth Assessment Report (AR4) and found that only 6 of the 18 models generated a reasonably realistic representation of monsoon precipitation climatology. For each of these six successful models, sea surface temperature (SST) and anomalous precipitation evolution along the equatorial Pacific during El Niño events displayed considerable differences when compared with observations. In short, most CGCMs do not simulate the spatial or interannual variation of monsoon precipitation accurately. Zhou and Yu (2006) showed that, over China, the estimated annual precipitation over East Asia exceeds the observed estimates in almost all models in AR4.

Higher spatial resolution is believed to improve a model's ability to simulate regional-scale precipitation patterns. For example, Kusunoki et al. (2006) found that the simulation of the mei-yu-changma-baiu rains in the EASM was improved substantially by increasing the horizontal resolution. Gao et al. (2006) reported that simulated large-scale precipitation patterns over East Asia are significantly affected by resolution, particularly during the mid-to-late monsoon months when smaller-scale convective processes dominate. In addition, complete and accurate representations of the physical processes involved, as well as of the real external forcing fields, are essential if realistic long-term variations are to be generated (i.e., the interdecadal variability or trend). For example, Duan and Wu (2009) evaluated the spatial pattern of the long-term trend in air temperature over Eurasia simulated by 16 CGCMs in IPCC AR4. Their results suggest that ozone, and the indirect effects of sulfate aerosol, may be important in reproducing the larger warming amplitude in the mid- and high latitudes and the resultant weakened Asian westerly jet (AWJ). Ongoing development since AR4 is expected to considerably improve the ability of the climate models to simulate monsoon precipitation patterns and variability resulting from the higher spatial resolution and more comprehensive physical schemes. This expectation must be validated by comparing the simulations in phase 5 of the Coupled Model Intercomparison Project (CMIP5) for the IPCC Fifth Assessment Report (AR5) to those in AR4. In particular, because of limited observations, the

complex topography, and the lack of inhabitants, the TPSM receives much less attention than either the EASM or SASM. Until now, a systematic evaluation of the skill of the models to simulate the circulation and precipitation associated with the TPSM has not been undertaken. Therefore, this study aims to investigate the performance of the state-of-the-art GCMs in reproducing the climate mean, interannual variability, and the trend in the TPSM over recent decades by comparing the simulations with the observational data and with each other. It will provide valuable information and useful insights for future model development, especially in very mountainous regions.

The remainder of this manuscript is organized as follows. In section 2, we provide a brief description of the data and models. Section 3 evaluates the TPSM in terms of climate mean circulation and precipitation simulated by the AGCMs and CGCMs for IPCC AR5. Section 4 investigates the interannual variability of the TPSM and its relationship with the EASM. Section 5 focuses on trends in the TPSM over recent decades in both simulations and observations, and section 6 contains the discussion and our conclusions.

2. Data and models

a. Data

The data used in this study were obtained from the following sources. First, regular surface meteorological observations between 1979 and 2005 from 105 stations at elevations above 2500 m for the TP region provided by the China Meteorological Administration (CMA). Variables include daily mean station surface pressure and daily accumulated precipitation. The precipitation of station is corrected by using the method from Ye et al. (2004). Second, monthly-mean air temperature and geopotential height records from 14 radiosonde stations on the TP archived by the CMA. These data were collected at 16 standard pressure levels (1000, 925, 850, 700, 500, 400, 300, 250, 200, 150, 100, 70, 50, 30, 20, and 10 hPa). As the surface of the TP is at almost 600 hPa, the levels selected for this study were limited to those from 500 to 20 hPa. Next, monthly-mean air temperature, geopotential height, and zonal and meridional wind speed fields from the National Centers for Environmental Prediction–National Center for Atmospheric Research (NCEP–NCAR) reanalysis data (Kalnay et al. 1996); the NCEP/Department of Energy (NCEP/DOE) Reanalysis 2 data (Kanamitsu et al. 2002); the Japan Meteorological Agency (JMA), who conducted the Japanese 25-yr Reanalysis (JRA-25; Onogi et al. 2007); and the European Centre for Medium-Range Weather Forecasts (ECMWF)

Interim Re-Analysis (ERA-Interim) data (Dee et al. 2011). The horizontal resolution is $2.5^{\circ} \times 2.5^{\circ}$ for the NCEP–NCAR and NCEP/DOE data at 17 standard pressure levels. For the JRA-25 data, the horizontal resolution is $1.25^{\circ} \times 1.25^{\circ}$, employing 23 standard pressure levels. For the ERA-Interim data, the horizontal resolution is $1.5^{\circ} \times 1.5^{\circ}$, employing 37 standard pressure levels. The NCEP–NCAR reanalysis dataset is available from 1948 to the present; the NCEP/DOE, JRA-25, and ERA-Interim datasets are available from 1979 to the present. Finally, monthly-mean precipitation data for the period 1979–2005 were obtained from the Global Precipitation Climatology Project, version 2.1 (GPCP; Adler et al. 2003), at a resolution of $2.5^{\circ} \times 2.5^{\circ}$.

b. Models

We analyzed the extensive integrations from 15 CGCMs and 8 of their atmospheric component models (i.e., AGCMs) that were based on the experiments designed by CMIP5 for IPCC AR5. The difference between AGCMs and CGCMs lies in the fact that SST and sea ice are prescribed by observation in the former, while they are generated by the models themselves in the latter. The horizontal resolution and forcing fields for the AGCMs and CGCMs are described in Table 1 (see for full list of model expansions). The horizontal grids of the GCMs vary from 192×288 (CCSM4) to 73×96 (HadCM3). The simulation scenario used was the Atmospheric Model Intercomparison Project (AMIP) run for AGCMs and the historical run for the CGCMs, in which the forcings are a combination of greenhouse gases, sulfate aerosols, ozone, black carbon, volcanic aerosols, and solar variability based on the data between 1979 and 2008 in the AMIP and between 1850 and 2005 in the CMIP. Well-mixed greenhouse gases (GHGs), tropospheric and stratospheric ozone, the direct effects of sulfate aerosol, and other forcings were included simultaneously in all 15 CGCMs, whereas the indirect effects of sulfate aerosol were incorporated in 12 of them (i.e., CanESM2, CCSM4, CNRM-CM5, CSIRO-Mk3.6.0, FGOALS-g2, FGOALS-s2, GISS-E2H, GISS-E2-R, HadCM3, IPSL-CM5A-LR, MRI-CGCM3, and NorESM1-M).

To facilitate the analysis and discussion of the impacts of resolution on model performance, the AGCMs and CGCMs were further sorted into a lower-resolution group that had global grids less than 16 200, which roughly equals $2^{\circ} \times 2^{\circ}$, and a higher-resolution group with global grids greater than 16 200. Similarly, the models were also classified according to whether the indirect effects of sulfate aerosol were included, with the aim of estimating its possible contribution. As most of the simulations based on the historical experiment

end in 2005 and the most significant trend in the observations, including the temperature and the surface wind speed over the TP, occurred after the 1970s (Duan and Wu 2008), the simulation results during the period 1979–2005 were compared both with each other and with the observations.

The Student's *t* test is employed to test whether the difference in climate means between the observation and models, the high-resolution group and the low-resolution group, and the both the direct and indirect effects (SA) group and sulfate direct (SD) group are significant. In spectrum analysis, the theoretical Markov spectrum and its upper confidence is taken to find the significant period. Following Ebert and McBride (2000), the *F* test is used to test the hypothesis that the pattern correlation coefficient is zero. To verify the significance of regression coefficients, the Student's *t* test is applied. The uncertainty of linear trend is showed by the confidence interval method. Unless stated otherwise, all significant differences, periods, correlations, and regressions reported in this study pass the 90% confidence level.

3. Climatology of the TPSM

a. General circulation and precipitation

In the upper troposphere, a prominent component of the circulation system of the Asian summer monsoon (ASM) is the planetary-scale high pressure system and the associated anticyclonic circulation. In summer [June–August (JJA) mean], the TP acts as a huge, strong, and elevated atmospheric heat source. In particular, the strong surface sensible heat flux makes the boundary layer very unstable and produces strong near-surface convergence, as well as upper-level divergence and negative vorticity. As a result, a surface heat low and the warm core of the Tibetan high develop over the TP (Fig. 1). Mason and Anderson (1963) found that the maximum Tibetan high appears close to the 100-hPa level, and its influence can extend from the Atlantic coast of Africa and across southern Asia to the Pacific Ocean. The ridge of the elongated Tibetan high typically occurs around 30°N and spans the entire Eastern Hemisphere from North Africa to the date line, with the core region covering the area of approximately 50° – 130°E and 15° – 40°N ; the ridge dominates the global upper-tropospheric circulation. The formation and maintenance of the Tibetan high are primarily attributed to the diabatic heating processes associated with deep convective rainfall in Southeast Asia and the western North Pacific and also to the sensible and convective heating over the TP (Wang 2006). The clockwise flow around the Tibetan high contains an easterly jet stream on its southern flank: the tropical easterly jet.

TABLE 1. Horizontal resolution and forcing fields for the historical and AMIP runs in CMIP5, with full model expansions. The horizontal resolution is the lat grid number multiplied by the lon grid number, and they are categorized into either low (<16 200) or high (>16 200) resolution groups according to their total grid number. The asterisk indicates that both the AGCM and CGCM runs are included and the forcing fields in the upper and lower lines for CGCM and AGCM, respectively. The abbreviations Nat, Ant, GHG, SD, SI, SA, TO, SO, Oz, LU, SI, VI, SS, Ds, BC, MD, OC, and AA denote the natural forcing (solar and volcanic), anthropogenic forcing (well-mixed greenhouse gases, aerosols, ozone, and land use change), well-mixed greenhouse gases, anthropogenic sulfate direct effects, anthropogenic sulfate indirect effects, anthropogenic sulfate direct and indirect effects, tropospheric ozone, stratospheric ozone, tropospheric and stratospheric ozone, land use change, solar irradiance, volcanic aerosol, sea salt, dust, black carbon, mineral carbon, and anthropogenic aerosols, respectively.

Models	Model expansion	Horizontal resolution	Group	Forcing	Sulfate effects
BCC-CSM1.1	Beijing Climate Center, Climate System Model, version 1.1	64 × 128 (8192)	Low	Nat, Ant, GHG, SD, Oz, SI, VI, SS, Ds, BC, OC	SD
CanAM4	Fourth Generation AGCM of the Canadian Centre for Climate Modelling and Analysis	64 × 128 (8192)	Low	Nat, Ant, GHG, SD, Oz, SI, VI, SS, Ds, BC, OC	SA
CanESM2*	Second Generation Canadian Earth System Model	64 × 128 (8192)	Low	GHG, Oz, SA, BC, OC, LU, SI, VI	SA
CCSM4	Community Climate System Model, version 4	192 × 288 (55 296)	High	SI, GHG, VI, SS, Ds, SD, BC, MD, OC, Oz, AA, LU	SD
CNRM-CM5*	Centre National de Recherches Météorologiques Coupled Global Climate Model, version 5	128 × 256 (32 768)	High	GHG, Oz, SA, BC, OC, LU, SI, VI	SA
CSIRO-Mk3.6.0	Commonwealth Scientific and Industrial Research Organisation Mark, version 3.6.0	96 × 192 (18 432)	High	GHG, SA, SI, VI, BC, OC	SA
FGOALS-g2*	Flexible Global Ocean–Atmosphere–Land System Model gridpoint, version 2	60 × 128 (7680)	Low	SI, GHG, VI, SS, Ds, SD, BC, MD, OC, Oz, AA, LU	SA
FGOALS-s2*	Flexible Global Ocean–Atmosphere–Land System Model, second spectral version	108 × 128 (13 824)	Low	GHG, Oz, SA, BC, Ds, OC, SS, SI, VI	SD
GISS-E2H	Goddard Institute for Space Studies Model E, coupled with the HYCOM ocean model	90 × 144 (12 960)	Low	GHG, SD, Oz, SI, VI, SS, Ds, BC, OC	SA
GISS-E2-R	Goddard Institute for Space Studies Model E, coupled with the Russell ocean model	90 × 144 (12 960)	Low	GHG, LU, SI, VI, BC, OC, SA, Oz	SA
HadGEM2-A	Hadley Centre Global Environment Model, version 2 (Atmosphere)	73 × 96 (7008)	Low	GHG, LU, SI, VI, BC, OC, SA, Oz	SA
HadCM3*	Hadley Centre Coupled Model, version 3	73 × 96 (7008)	Low	Ant, Nat (all forcings)	SA
IPSL-CM5A-LR	L'Institut Pierre-Simon Laplace Coupled Model, version 5, coupled with NEMO, low resolution	96 × 96 (9216)	Low	GHG, Oz, SA, SI, VI	SA
INM-CM4.0	Institute of Numerical Mathematics Coupled Model, version 4.0	120 × 180 (21 600)	High	Nat, Ant, GHG, SA, Oz, LU, SS, Ds, BC, MD, OC, AA	SA
MPI-ESM-LR*	Max Planck Institute Earth System Model, low resolution	96 × 192 (18 432)	High	GHG, Oz, SA, BC, Ds, OC, SS, SI, VI	SD
MRI-CGCM3*	Meteorological Research Institute Coupled Atmosphere–Ocean General Circulation Model, version 3	160 × 320 (51 200)	High	GHG, Oz, SD, SI, VI, LU	SA
NorESM1-M*	Norwegian Earth System Model, version 1 (intermediate resolution)	96 × 144 (13 824)	Low	GHG, SA, Oz, LU, SI, VI, BC, OC	SA

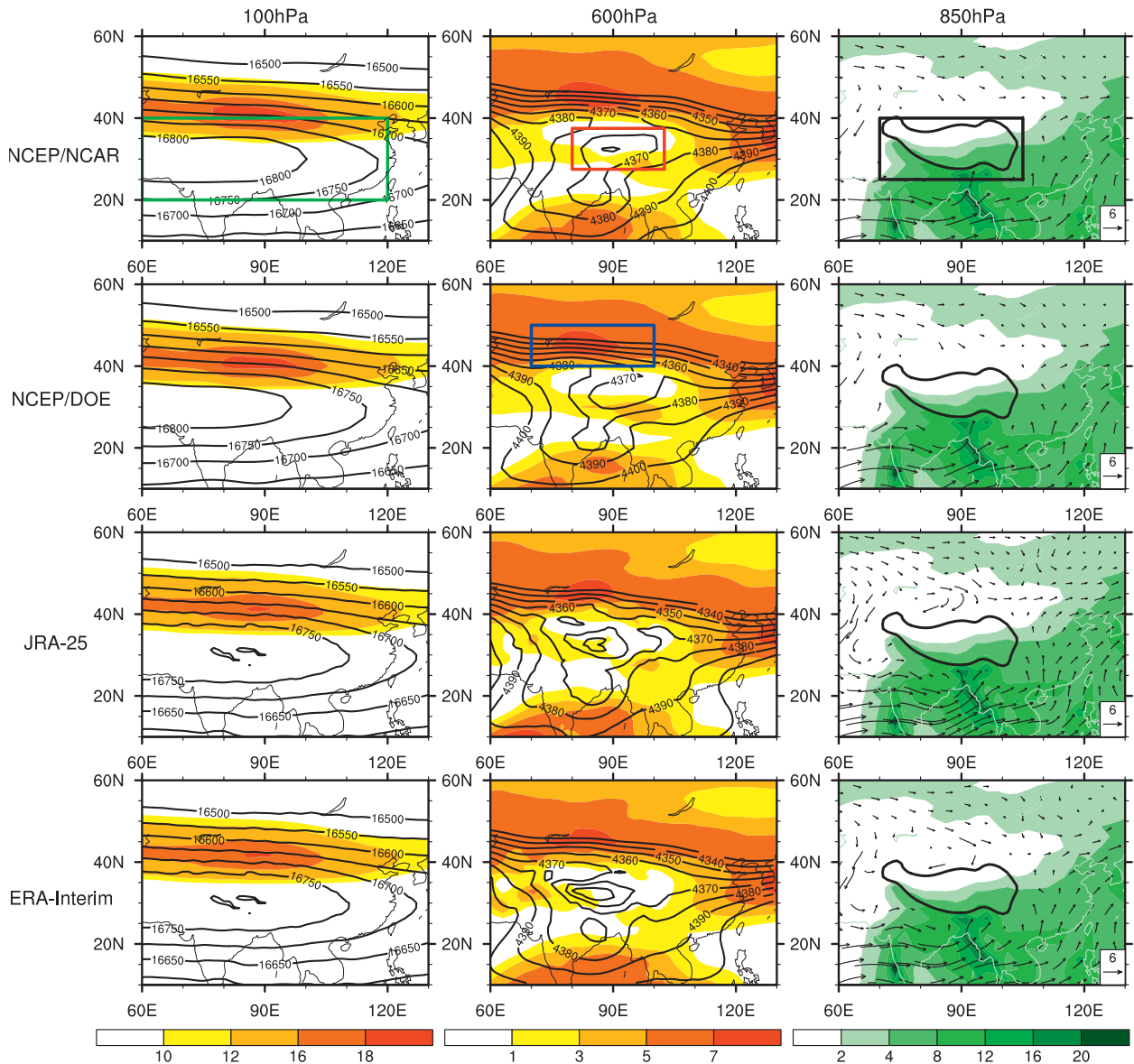


FIG. 1. The 1979–2005 JJA mean geopotential height (contours, gpm) and zonal wind speed (shaded, $\text{m}\cdot\text{s}^{-1}$) at (left) 100 and (center) 600 hPa and (right) 850-hPa wind vectors from four reanalysis datasets, together with GPCP precipitation fields (shaded, $\text{mm}\cdot\text{day}^{-1}$). The green, red, black, and blue boxes denote the Tibetan high, the TP surface heat low, the TP, and the AWJ domains, respectively.

In the upper troposphere and lower stratosphere, the AWJ around the midlatitudes is a narrow belt of strong westerly winds with large horizontal and vertical wind shears over subtropical East Asia (Sheng 1986). The AWJ exhibits significant seasonal evolutions in its intensity and location. The axis and center of the AWJ are located at 200 hPa and reach their southernmost position in March and their northernmost position in August. The central intensity of the AWJ is about $70 \text{ m}\cdot\text{s}^{-1}$ in winter and $35 \text{ m}\cdot\text{s}^{-1}$ in summer. From winter to summer, the axis experiences two northward jumps (Yeh et al. 1958). This jet stretches from the western Pacific

to the west coast of North America. Because of the topographic blocking effect, the AWJ in the mid- and lower troposphere is divided into two branches that flow along the northern and southern flanks of the TP before merging again downstream and maintaining the westerly jet belt over the northwest Pacific.

Near the surface, the strong sensible heat source generates airflow convergence and a heat low over the TP. The surface heat low becomes established in May, and reaches a maximum in July and August, before dissipating again in October (Yeh and Gao 1979). At 850 hPa, the southwesterly jet to the southeast of the TP meanders

from the tropical monsoon regions to northern China and the Korean Peninsula and supplies abundant moisture to the EASM. Our early results, from both data analysis and numerical simulations, suggested that the thermal forcing of the TP substantially intensifies this low-level southwesterly during spring and summer (i.e., Duan and Wu 2005; Wu et al. 2012). The monsoon regions are sometimes defined by precipitation amounts (e.g., Wang and LinHo 2002; Zeng and Lu 2004). The right panels of Fig. 1 show that, besides the SASM and EASM regions, the daily accumulative precipitation over the southern and eastern TP in summer also reaches 4 mm-day^{-1} , providing further support for the occurrence of a monsoon over the TP.

A reasonable approximation of the climatic mean circulation and precipitation is required if the GCMs are to generate rational simulations of climate variability. Figures 2 and 3 show the difference fields for the JJA mean circulation and precipitation between simulations and observations. All of the AGCMs and CGCMs mimic the TPSM circulation system well, including the surface heat low and the Tibetan high, with the pattern correlation significant at the 95% confidence level. Because of the high degree of similarity in the climatology among all reanalysis datasets, here we only show the difference fields between the JRA-25 data and simulations. Also, all fields were interpolated onto the regular $2.5^\circ \times 2.5^\circ$ grid for ease of comparison. The ensemble of simulated Tibetan high is weaker in its southern part and the surface heat low is slightly stronger than in the reanalysis data. In contrast, the southwesterly at 850 hPa in East Asia is clearly stronger than in the observations, especially in the AGCMs. In the midtroposphere, the simulated 600-hPa western Pacific subtropical high (WPSH) typically shifts northward to some extent. Besides the impact of model resolution, this bias in the monsoon circulation might also be related to the significant warm bias in the land surface temperature over Eurasia in the AGCMs and the cold bias in SST over the neighboring oceans in the CGCMs (figures not shown). This bias further enhances the land–sea thermal contrast and the resultant stronger large-scale monsoon circulation in the lower atmosphere. Typically, the bias in the monsoon precipitation pattern is very similar in both the AGCMs and CGCMs; that is, precipitation is overestimated in the tropical oceans and the southern and eastern TP but underestimated in the northern SASM and EASM regions. The horizontal resolution seems to have no significant impact on the climate mean circulation at 100 hPa, but affects the tropical and subtropical precipitation distribution, whereas the indirect effects of sulfate in the CGCM's group influence the 600-hPa circulation over the TP obviously. Generally, the pattern

correlation in circulation and precipitation between the observations and simulations in both the AGCM's and CGCM's groups are significant at the 95% confidence level, and the correlation coefficients are slightly larger in the higher resolution group and the group in which the indirect aerosol effects are included.

To more precisely demonstrate model performance in simulating circulation and precipitation in the TPSM, the Taylor diagram (Taylor 2001) is shown in Fig. 4, which highlights the spread between models and observations in the JJA mean 100-hPa Tibetan high, 600-hPa surface heat low, and TP precipitation. The Taylor diagram provides a concise statistical summary of how well patterns match each other in terms of their correlation, their root-mean-square difference, and the ratio of their variances. Generally, it is difficult to select just one or two models that always perform well in all respects. Whereas the CanAM4, FGOALS-s2, CNRM-CM5, and HadGEM2-A models in the AGCM's group simulate TP precipitation better, with spatial correlation coefficients higher than 0.6 and a relatively small variance difference when compared with the observations, in the CGCM's group the simulated TP precipitation in CNRM-CM5, CanESM2, FGOALS-s2, BCC-CSM1.1, HadCM3, and INM-CM4.0 seems to be superior to the others. By further comparing the skill score for both circulation and precipitation from the AGCMs with the CGCM's groups, we found that the performance of a CGCM depends directly on its atmospheric component (tables are omitted here), suggesting the overwhelming role of the AGCM in climate model development.

b. Annual cycle of precipitation

In addition to the seasonal-mean state, the annual cycle is another aspect with which to evaluate model performance with respect to monsoon precipitation. Here, we use the monsoon precipitation index (MPI) to characterize the annual cycle of TP precipitation, which is defined by Wang and Ding (2008) as the ratio between the annual range of precipitation (May–September minus November–March) and the annual-mean precipitation. Larger values of MPI usually indicate a stronger monsoon climate. Figure 5 presents the MPI difference fields between the simulations and the GPCP data. The MPI pattern correlation coefficients between the simulations and observation in all models are above 0.8 and exceed the 95% confidence level, indicating that the ability of the models to simulate the seasonal evolution of precipitation over and around the TP is acceptable. However, the proportion of summer monsoon precipitation is systematically underestimated over the western TP and to its north and south sides by almost all GCMs. It is noteworthy that a higher resolution, and the inclusion

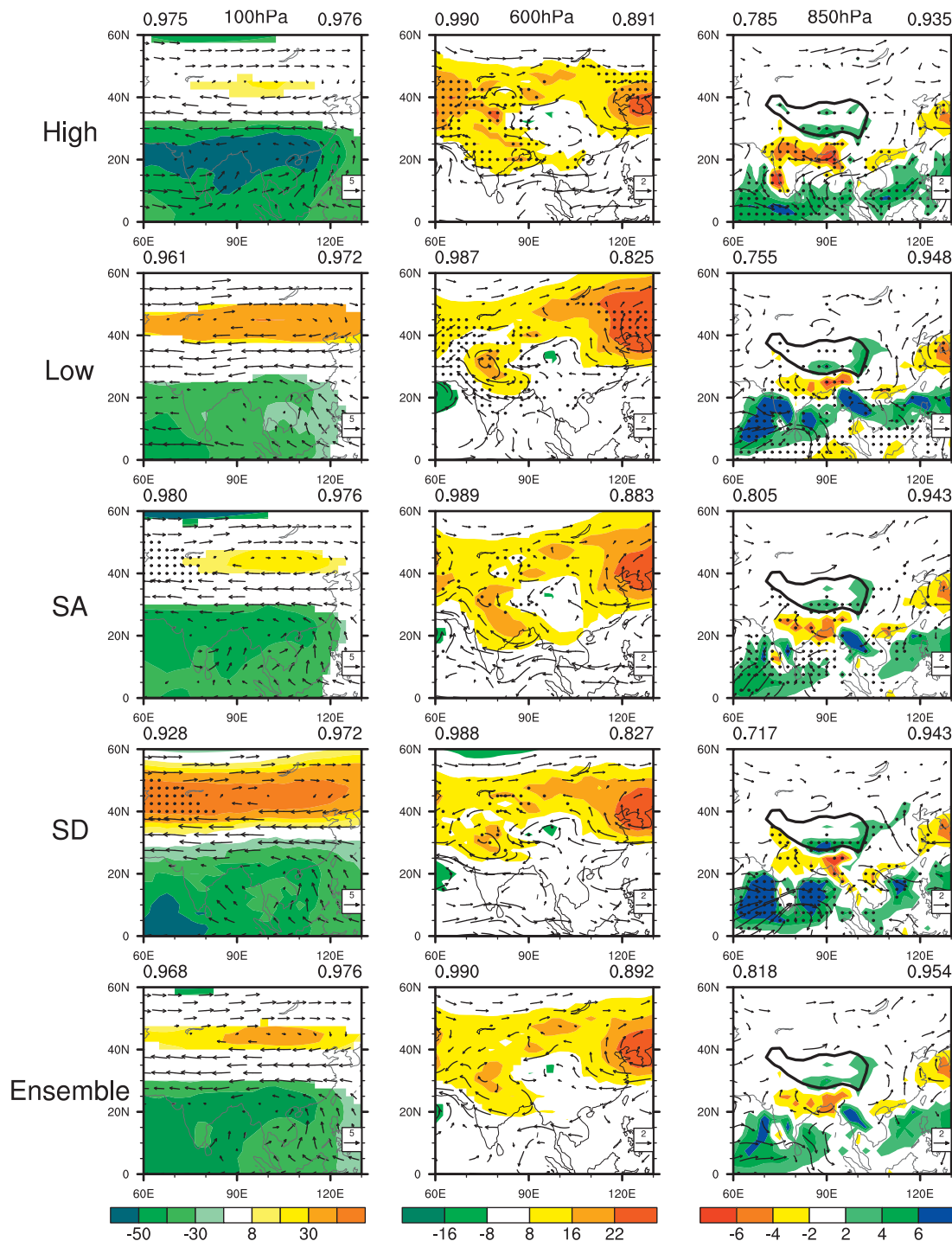


FIG. 2. The difference fields between the AGCMs and JRA-25 reanalysis data for 1979–2005 mean JJA wind vectors ($\text{m}\cdot\text{s}^{-1}$) and geopotential height (shaded, gpm) at (left) 100 and (center) 600 hPa and (right) 850-hPa wind vectors and precipitation difference between the AGCMs and GPCP (shaded, $\text{mm}\cdot\text{day}^{-1}$), which are statistically significant at the 90% level. The high, low, SA, SD, and ensemble panels denote the model group of high and low horizontal resolution, with both sulfate direct and indirect effects included, with only sulfate direct effects included, and all models ensemble mean, respectively. The dotted areas indicate the difference of geopotential height or precipitation between high and low (SA and SD) are statistically significant at the 90% level. For the left and center panels, the pattern correlation coefficients in zonal wind speed between simulations and JRA-25 are listed in top right and the pattern correlation coefficients in geopotential height are listed in top left. Similarly, the pattern correlation coefficients in precipitation between simulations and GPCP are also shown in the top left for the right panels.

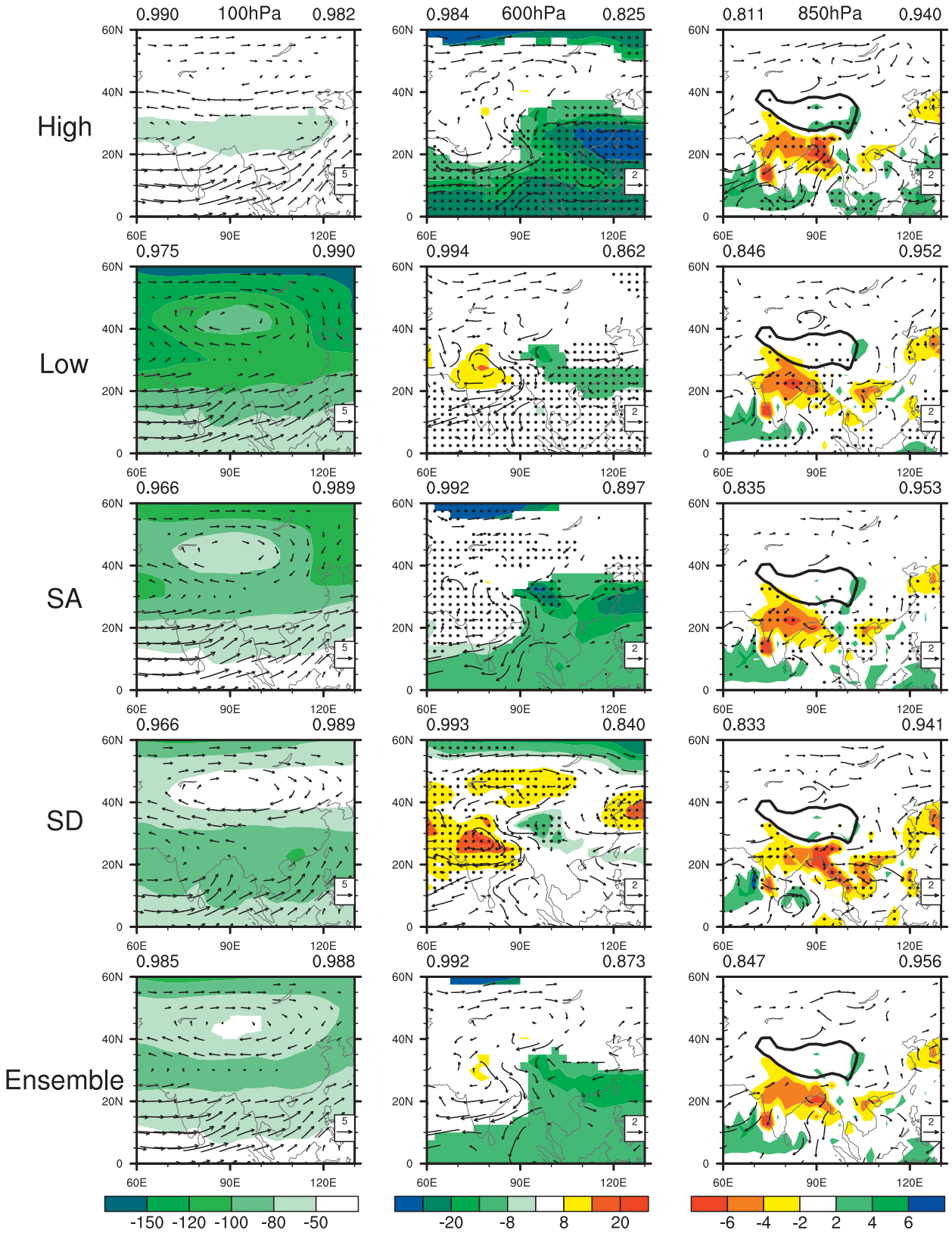


FIG. 3. As in Fig. 2, but for CGCMs.

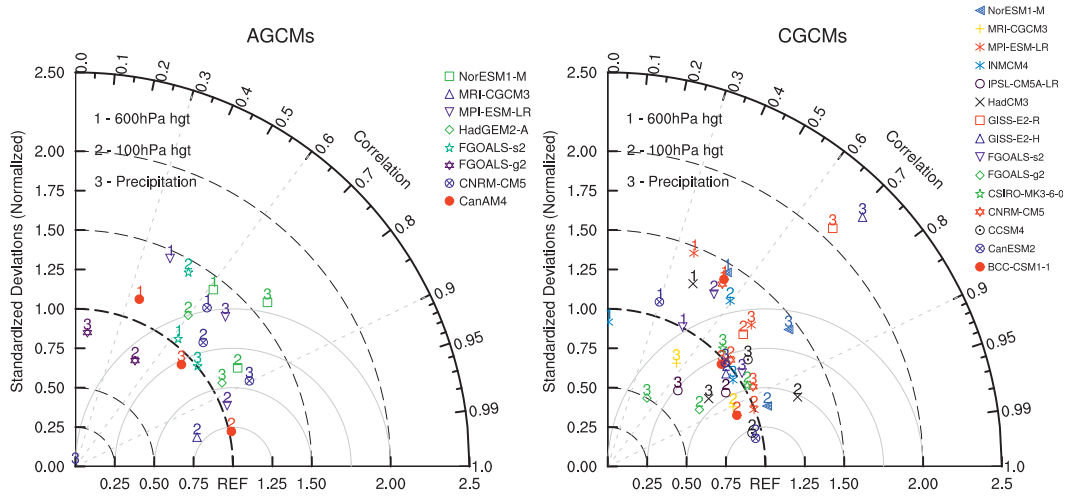


FIG. 4. Taylor diagrams that summarize the pattern statistics between the simulations and observations for the normalized JJA mean circulation and precipitation related to the TPSM in 1979–2005. The radial distance from the origin indicates the ratio between standard deviation of each model simulation and standard deviation of the observation. The angle from the horizontal axis represents the spatial correlation between the simulation of a certain model and the observation. The GPCP data and JRA-25 reanalysis are chosen for the observed precipitation and circulation. As in Fig. 1, the colors green, red, and black define the domain of the 100-hPa Tibetan high, 600-hPa surface heat low, and TP precipitation, respectively. Note that in some models, data are absent at 600 hPa and the corresponding results are not shown here.

of the indirect effects of sulfate, does help to reduce the bias in the annual cycle of precipitation in both AGCMs and CGCMs, not only in the magnitude, but also in the spatial distribution, as revealed by the pattern correlation coefficients. This conclusion is essentially consistent with previous results documented in IPCC AR4 (2007).

4. Interannual variability of the TPSM

The TPSM shows large amplitude fluctuations over various time scales. Among the wide range of time scales, the interannual variability is the most extensively investigated because of the clearly evident differences from year to year and the direct socioeconomic impacts on local inhabitants.

a. Circulation

To clearly describe monsoon variability, it is necessary to specify the time and location of the monsoon circulation. The variation of the Tibetan high can be defined by the intensity index of the 100-hPa geopotential height within the area 20°–40°N, 60°–120°E (the green rectangle in the top left panel of Fig. 1). Similarly, the surface heat low index over the TP is defined by the 600-hPa geopotential height within the area 27.5°–37.5°N, 85°–105°E (the red rectangle in the top middle panel of Fig. 1). As the interannual variability of the surface heat low and the Tibetan high in different reanalysis datasets are very similar (figure omitted), in this and following

sections of the paper we use the JRA-25 data to represent the observed circulation. Note that all linear trends in both the data and simulations have been removed in this section.

Table 2 contains the correlation coefficients of the indices of the surface heat low and the Tibetan high between the simulations and observations over the period 1979–2005. In the CGCM’s group, the Tibetan high index is significantly correlated with the observational data only in CCSM4, IPSL-CM5A-LR, and MPI-ESM-LR, and no CGCM generated an interannual variability in the surface heat low that was similar to the observations. In the AGCM’s group, the simulated interannual variability was much better. The Tibetan high intensity index in all of the AGCMs was significantly correlated with the observational data, except for models HadGEM2-A and NorESM1-M. Moreover, the surface heat low index in CanAM4 and FGOALS-s2 was significantly correlated with the observations. Note that data at 600 hPa were available for only five AGCMs. Thus, interannual variability in the surface heat low was reproduced by almost half of the AGCMs; in the other three, although the correlation was not statistically significant, a positive correlation was found, particularly in MPI-ESM-LR and NorESM1-M.

The variability of the TPSM is largely controlled by the internal dynamics of the atmosphere, but the slowly varying boundary forcing from the underlying land and surrounding oceans also plays an important role. The

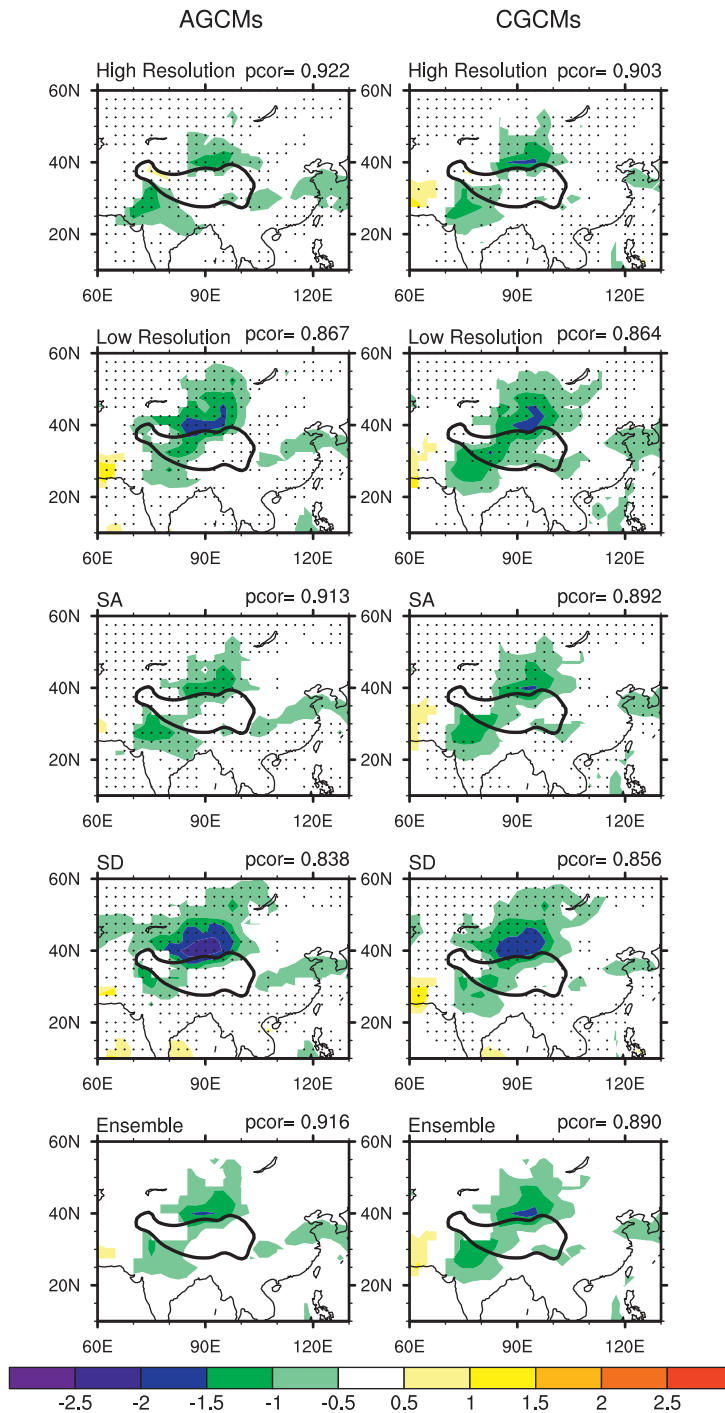


FIG. 5. The difference fields of 1979–2005 mean MPI between the simulations and GPCP data, which are statistically significant at the 90% level. The dotted areas indicate the grids of MPI difference between high and low (SD and SA) are statistically significant at the 90% level. The pattern correlation coefficients of MPI between simulations and GPCP are listed in the top right for each panel.

TABLE 2. Correlation between simulated and observed indices of the surface heat low over the TP and the Tibetan high. Confidence levels are indicated as 90% (*), 95% (**), and 99% (***). No value indicates no data.

Models	Surface low		Tibetan high	
	AGCM	CGCM	AGCM	CGCM
BCC-CSM1.1	—	-0.250	—	0.279
CanAM4/CanESM2	0.327*	0.013	0.485**	0.211
CCSM4	—	—	—	0.433**
CNRM-CM5	0.032	-0.169	0.472**	0.273
CSIRO-Mk3.6.0	—	—	—	-0.071
FGOALS-g2	—	—	0.365*	0.184
FGOALS-s2	0.408**	0.014	0.478**	0.168
GISS-E2H	—	—	—	0.277
GISS-E2-R	—	—	—	0.156
HadGEM2-A/HadCM3	—	-0.044	0.074	0.247
IPSL-CM5A-LR	—	—	—	0.419**
INM-CM4.0	—	-0.280	—	-0.025
MPI-ESM-LR	0.237	0.218	0.533***	0.356*
MRI-CGCM3	—	—	0.572***	0.023
NorESM1-M	0.232	-0.101	0.316	0.234

classical concept of the monsoon as a circulation system driven by the thermal contrast between oceans and continents implies the importance of ocean and land surface processes to the monsoon and its variability. Therefore, it is not surprising that the AGCM's group forced by the observed SST reproduces interannual variability that is closely comparable to that observed in nature. In addition, the lower overall skill in the simulation of the surface heat low compared with the Tibetan high may be related to the much smaller scale of the former and its greater sensitivity to the topography and thermal conditions at the surface.

However, almost all of the models were unable to adequately capture the periodic signal of the TPSM. Zhang et al. (2000) reported a quasi-4-yr period in the Tibetan high, and Figs. 6 and 7 show the power spectra for the indices of the surface heat low and the Tibetan high based on the JRA-25 data and simulations. A significant quasi-4-yr period in the surface heat low can be detected in the JRA-25 data, but such a significant period was only reproduced by one AGCM (i.e., FGOALS-s2), and no significant period exists in other AGCMs. This is also the case for the CGCM's group, except that INM-CM4.0 generated a quasi-5-yr period. Coherent with the low-level circulation, a 4–6-yr period in the Tibetan high was seen in some AGCMs (e.g., CanAM4, FGOALS-s2, FGOALS-g2, and HadGEM2-A) and two CGCMs (INM-CM4.0 and MRI-CGCM3), despite the low significance of the quasi-4-yr period in the JRA-25 reanalysis data. The interannual variability of TP precipitation was not significant in either the observations or the simulations (figures not shown here).

b. Relationship between the TPSM and EASM

Previous studies suggest that the interannual variability of the TPSM and the corresponding thermal forcing exert a significant impact on the EASM (e.g., Duan et al. 2005; Zhao et al. 2010). To address whether this relationship also exists in the models, in Figs. 8 and 9 we plot the regression fields of the 600-hPa wind vector and precipitation upon the TPSM index defined by Tang (1995) in both data (wind vector from JRA-25 and precipitation from GPCP) and simulations. The TPSM index is calculated from the geopotential height difference between the four boundary points (32.5°N, 80°E; 25°N, 90°E; 32.5°N, 100°E; and 40°N, 90°E) and the midpoint (32.5°N, 90°E), which generally represent the activity of the surface heat low over the TP. The correlation coefficient between the TPSM index and the domain-averaged precipitation over the central and eastern TP (27.5°–37.5°N, 80°–90°E) during 1979–2005 is 0.49, above the 99% significance level, and that between the TPSM index and the domain-averaged 600-hPa geopotential height over the TP (27.5°–37.5°N, 85°–105°E) is -0.41, above the 95% significance level; whereas the TPSM index shows a moderate positive correlation with the Tibetan high, with a correlation coefficient of 0.27 (just above 80% confidence level). In the JRA-25 wind fields and the GPCP precipitation data, a positive TPSM index denotes a cyclonic circulation and abundant precipitation over the southeastern TP. In the EASM region, southerly winds from the tropics and northerlies from the mid- and high latitudes converge to the east of the plateau and the mid- and lower Yangtze River, corresponding to the positive precipitation anomaly between 25° and 35°N but negative precipitation anomaly in north China. This typically denotes a weak EASM (e.g., Guo 1983; Lau et al. 2000; Zhang et al. 2003). In the southern SASM regions and the South China Sea, the low-level circulation is characterized by an anticyclonic circulation anomaly and deficient precipitation. These observations imply that a seesaw pattern exists between the TPSM and EASM or SASM with respect to their interannual variability. In the models, the coherent relationship between the TPSM index and precipitation over the southeastern TP occurs in all five AGCMs with valid data at 600 hPa, whereas the opposite interannual variability between the TPSM and EASM or SASM is evident only in CNRM-CM5. In the CGCM's group, almost no one can reproduce this relationship. Therefore, the interannual variability of either the TPSM or ASM is still not adequately simulated by the current GCMs. This may be related to the bias in the climate mean circulation and precipitation fields (i.e., the underestimated monsoon precipitation and

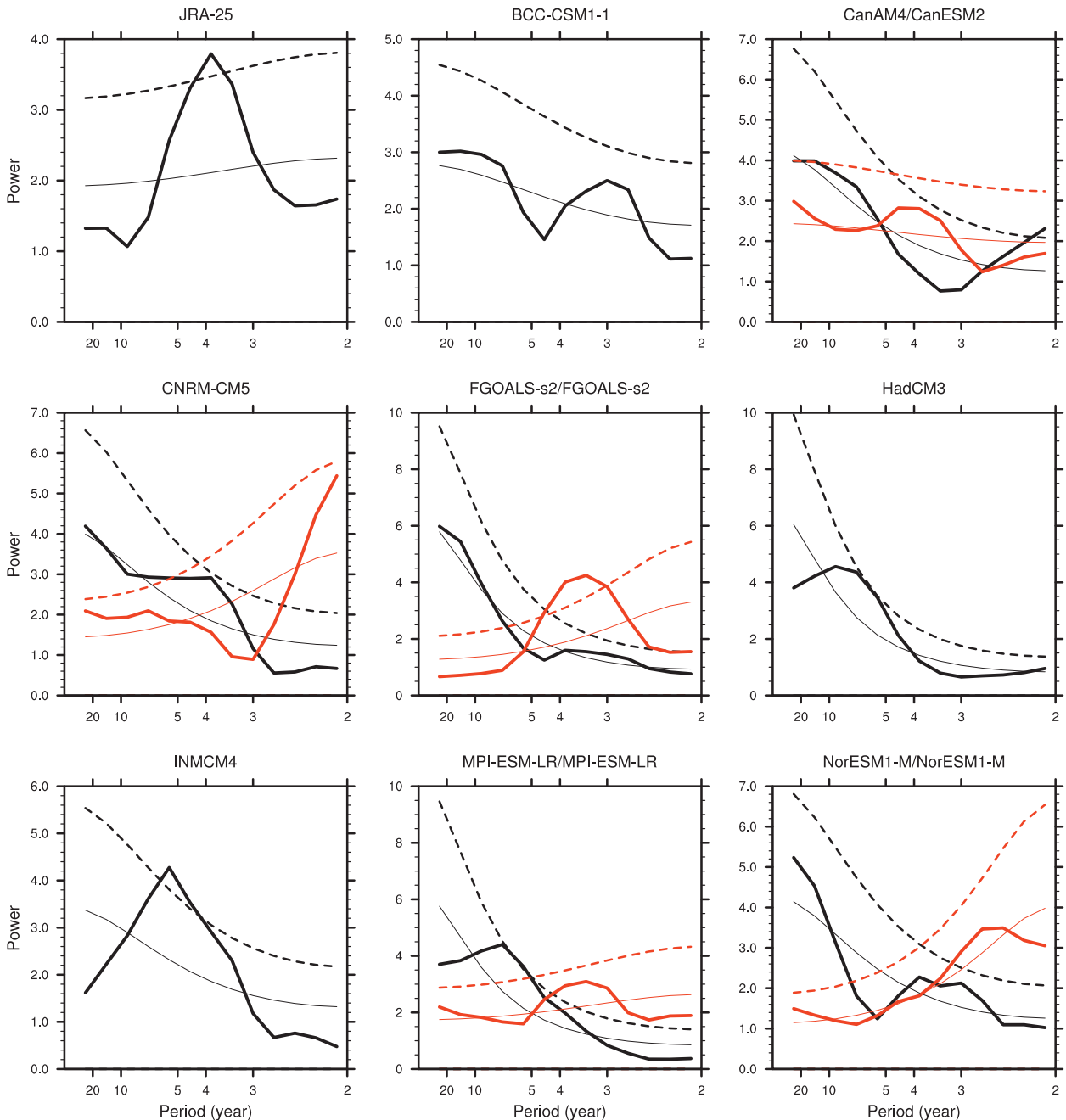


FIG. 6. The power spectrum analysis of the normalized index of the TP surface heat low in JRA-25, the AGCMs (red lines), and the CGCMs (black lines) during 1979–2005. The dashed and thin solid lines represent the 90% confidence level and red noise, respectively.

the overestimated low-level southwesterly in models over the EASM region described above).

5. TPSM trends over recent decades

Tang (1995) found that the TPSM has experienced significant decadal changes in the twentieth century, with a period of about 34 years. Before 1968, and after

1984, the TPSM was in a positive phase, while a negative phase occurred between 1968 and 1984. As the record of reliable meteorological observations over the TP is too short to adequately investigate the interdecadal variability of the TPSM, here we only discuss its linear trend during recent decades. We plotted the normalized time series of the JJA mean 600-hPa geopotential height index and the precipitation index for the entire TP based

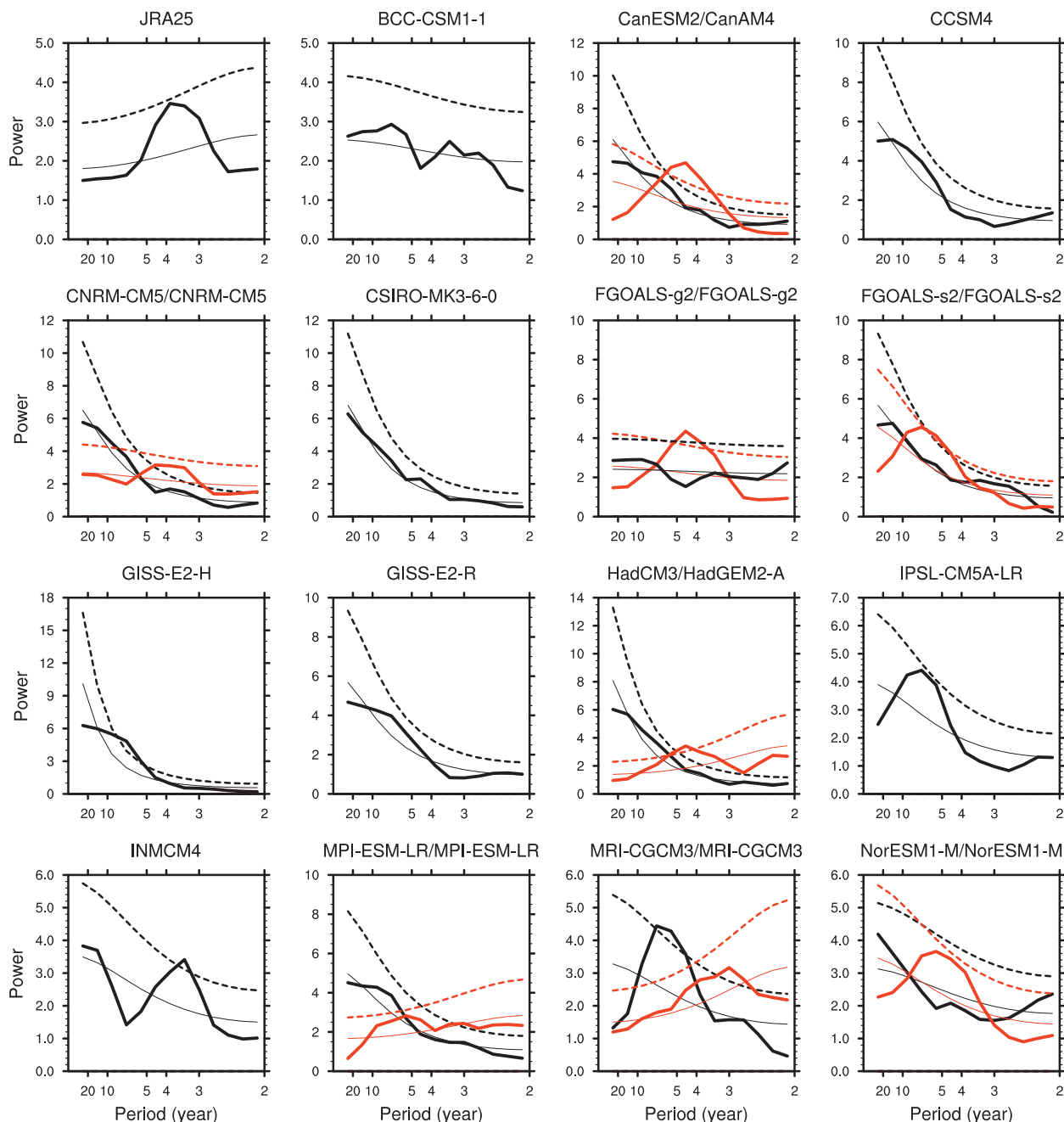


FIG. 7. As in Fig. 6, but for the Tibetan high.

on the average of the historical records from 105 stations together with the 100-hPa geopotential height index based on the average of data from 14 radiosonde stations between 1979 and 2005 (Fig. 10). The precipitation index shows an increasing trend ($0.041 \text{ mm day}^{-1} \text{ decade}^{-1}$), indicating an enhanced TPSM, although the trend is not statistically significant. Meanwhile, the 600-hPa geopotential height over the TP shows an upward trend ($3.462 \text{ gpm decade}^{-1}$ above the 95% significance level),

implying a weakening trend in the surface heat low. This phenomenon should be directly related to the substantial surface warming and the suppressed in situ sensible heat source (Duan and Wu 2008). At 100 hPa, as in the case of the surface heat low, the Tibetan high shows a distinct decreasing trend ($-13.72 \text{ gpm decade}^{-1}$ above the 95% significance level). The opposing trends of precipitation and the surface heat low are not contradictory because the precipitation change over the TP is not significant,

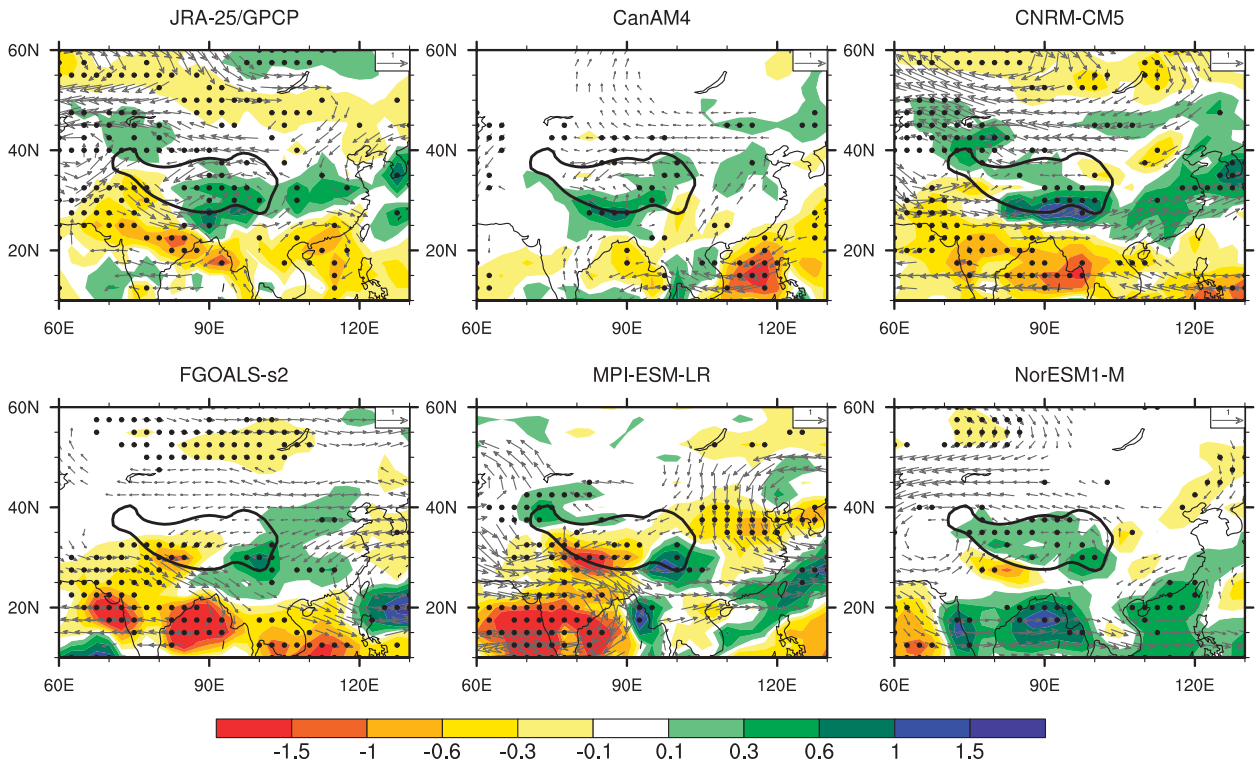


FIG. 8. The regressed fields of 600-hPa wind vector (gray, m s^{-1} ; statistically significant under the 90% level are masked) and precipitation (shaded, mm day^{-1} ; black dotted areas indicate the grids statistically significant above the 90% level) upon the TP monsoon index in the observations (wind in JRA-25 and precipitation in GPCP) and five AGCMs.

and the pattern shows an appreciable spatial heterogeneity; that is, it increases in the northern and southern TP but decreases in the mid-TP (Duan et al. 2008).

Quantitative changes in the surface heat low and the Tibetan high between 1979 and 2005, simulated by both AGCMs and CGCMs, are shown in Table 3. Clearly, all AGCMs and CGCMs having data at 600 hPa can reproduce the upward trend of the geopotential height during the last decades, and most of the simulated trends exceed the 99% confidence level, although the amplitude is obviously larger than the observations. However, in the upper troposphere the 100-hPa geopotential height over the TP also follows a significantly upward trend in all models, and this differs markedly from the observational data.

Vertical climate change over the TP during recent decades is characterized by warming in the mid- and lower troposphere but cooling in the upper troposphere and lower stratosphere, corresponding to the increased (decreased) geopotential height in lower (upper) layers (Duan et al. 2006). Figure 11 shows the JJA mean temperature profile and its linear trend over the TP from 1979 to 2005 in both the data and simulations. Radiosonde observations indicate that the tropopause over the TP

appears at 70 hPa, which is fairly consistent with the JRA-25 data and all GCMs. This demonstrates the ability of the models to simulate the climate mean vertical profile of the atmosphere. The change in temperature profile is characterized by a clear warming trend below 250 hPa but a much larger cooling trend above this level and up to 20 hPa in both the radiosonde and JRA-25 data. The maximum warming trend (about $0.1^{\circ}\text{C decade}^{-1}$ in the radiosonde data and $0.3^{\circ}\text{C decade}^{-1}$ in the JRA-25 data) occurs at 400 hPa. The cooling trend at 100 hPa corresponds to the weakening of the Tibetan high as shown in Fig. 10. However, in simulations, the vertical profile of the temperature trend over the TP shows some differences to the observations. The uniform warming trend in most of the models extends to 150 hPa and even up to 100 hPa in some cases. Typically, the simulated warming (cooling) trend in the mid- and lower troposphere (upper troposphere and lower stratosphere) is about twice as large as the observations. Such a warming bias in the upper atmosphere might be relevant to the processes controlling the moisture profile, cloud response to global warming, and ozone in the stratosphere, and further study is necessary to address this issue in the future.

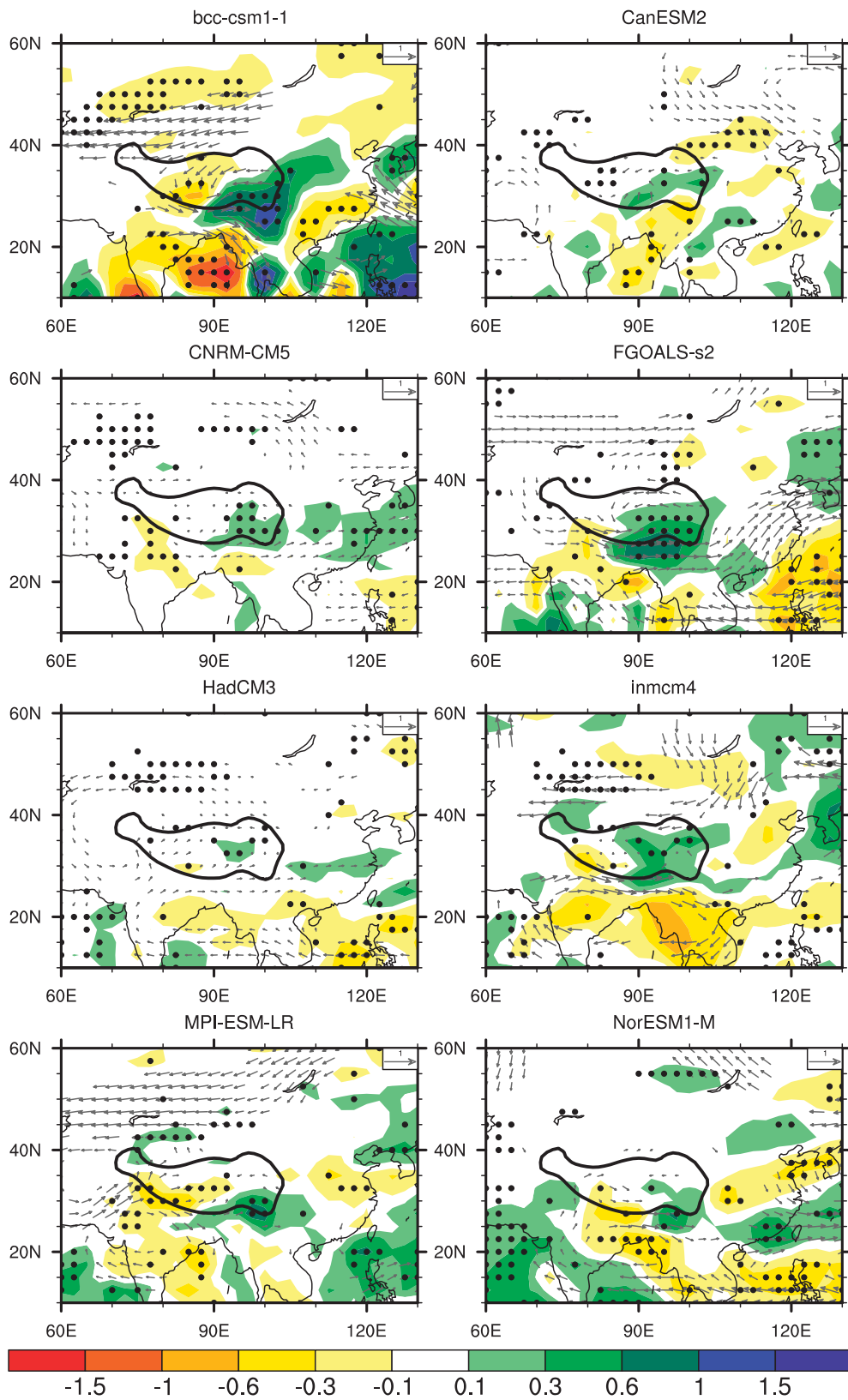


FIG. 9. As in Fig. 8, but for eight CGCMs.

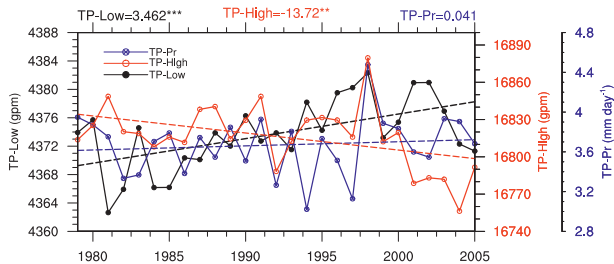


FIG. 10. The time series and the corresponding linear trends of the 105 station-averaged precipitation (TP-Pr; blue, $\text{mm day}^{-1} \text{decade}^{-1}$) and the 600-hPa geopotential height (TP-Low; black, gpm decade^{-1}), together with the 100-hPa geopotential height averaged by 14 radiosonde stations (TP-High; red, gpm decade^{-1}) over the TP in summer during 1979–2005. The trends are listed at the top of the panel. Confidence levels are indicated for 95% (**) and 99% (***)

It seems reasonable to assume that the current state-of-the-art climate models incorporate improved dynamical frameworks and a better understanding of the relevant physical processes when compared with those used in IPCC AR4. So, can we expect a more reasonable simulation of regional climate change around the TP? To address this question, we plotted the observed and simulated linear trends of the 500-hPa AWJ indices and the corresponding linear trends between 1979 and 2005 (Figs. 12). In the observations, there is a meridional asymmetry in climate warming over Eurasia [i.e., a more pronounced warming trend in mid- and high latitudes than in the subtropics and a consequent decline in the AWJ (Duan and Wu 2009)]. The trend in the AWJ is $-0.44 \text{ m s}^{-1} \text{decade}^{-1}$ in the JRA-25 data at the 95% confidence level (Fig. 12). This feature was successfully reproduced by all eight AGCMs, and half of them (i.e., CNRM-CM5, FGOALS-g2, FGOALS-s2, and MRI-CGCM3) passed the significance test. In the CGCM's group, 10 of the 15 CGCMs reproduced the weakening trend in the AWJ, and four CGCMs (i.e., CanESM2, CNRM-CM5, CSIRO-Mk3.6.0, and GISS-ES-R) passed the significance test. Such a discrepancy might impact the simulated EASM trend because the circulation and precipitation patterns are closely related to the location and intensity of the AWJ. In IPCC AR4, 6 of the 16 CGCMs reflected this asymmetric warming amplitude and the weakened AWJ at 500 hPa over Eurasia (Duan and Wu 2009). Consequently, the warming pattern over Eurasia simulated by the CGCMs in CMIP5 has been improved to a certain extent when compared with that in AR4.

Furthermore, it seems that no direct relationship exists between model resolution and the ability to reproduce the regional warming pattern. Notice that the common forcing fields of greenhouse gases, sulfate aerosol direct effects, black carbon, and tropospheric

TABLE 3. Simulated linear trends (gpm decade^{-1}) in the surface heat low and the Tibetan high from 1979 to 2008. Significance levels are indicated as 90% (*), 95% (**), and 99% (***). No value indicates no data.

Models	Surface low		Tibetan high	
	AGCM	CGCM	AGCM	CGCM
BCC-CSM1.1	—	3.010	—	25.99***
CanAM4/CanESM2	3.107***	5.747***	19.91***	27.42***
CCSM4	—	—	—	24.72***
CNRM-CM5	5.872***	3.557***	16.42***	16.74***
CSIRO-Mk3.6.0	—	—	—	19.84***
FGOALS-g2	—	—	17.60***	12.16***
FGOALS-s2	4.150***	4.779***	18.27***	17.98***
GISS-E2H	—	—	—	11.14***
GISS-E2-R	—	—	—	12.43***
HadGEM2-A/ HadCM3	—	3.921***	7.721	21.12***
IPSL-CM5A-LR	—	—	—	34.63***
INM-CM4.0	—	0.276	—	6.097
MPI-ESM-LR	5.049***	5.283***	18.98***	17.54***
MRI-CGCM3	—	—	18.08***	5.095**
NorESM1-M	3.814***	3.051***	20.83***	18.80***

and stratospheric ozone fields have been imposed in all models, and the sulfate aerosol indirect effects are also simultaneously included in 12 CGCMs. The role of sulfate aerosol indirect effects in influencing ASM activity and climate change during the last half of the twentieth century has been emphasized separately by Qian and Giorgi (1999), Xu (2001), Lau et al. (2008), and Duan and Wu (2009). However, in this work all three CGCMs without the aerosol indirect effects included have also reproduced the weakened AWJ. This implies that more emphasis should be placed on other factors when simulating the regional temperature trends in the models. Most recent numerical simulation results from Guo et al. (2012) also indicated that the EASM was not significantly changed as either SO_2 or black carbon emissions increased from 1950 to 2000 levels.

6. Summary and discussion

In this study, the extensive integrations produced for CMIP5 from the historical runs of 15 CGCMs and AMIP runs from eight AGCMs were used to evaluate the performance of state-of-the-art GCMs in simulating the climatology, annual cycle, interannual variability, and trend of the TPSM. Results from the multimodel intercomparison indicate that all of the GCMs are able to successfully simulate the climate mean TPSM circulation systems, including the surface heat low over the TP and the Tibetan high above it. However, no single model consistently performed well in all aspects of the simulation, and a large bias still exists in the climate

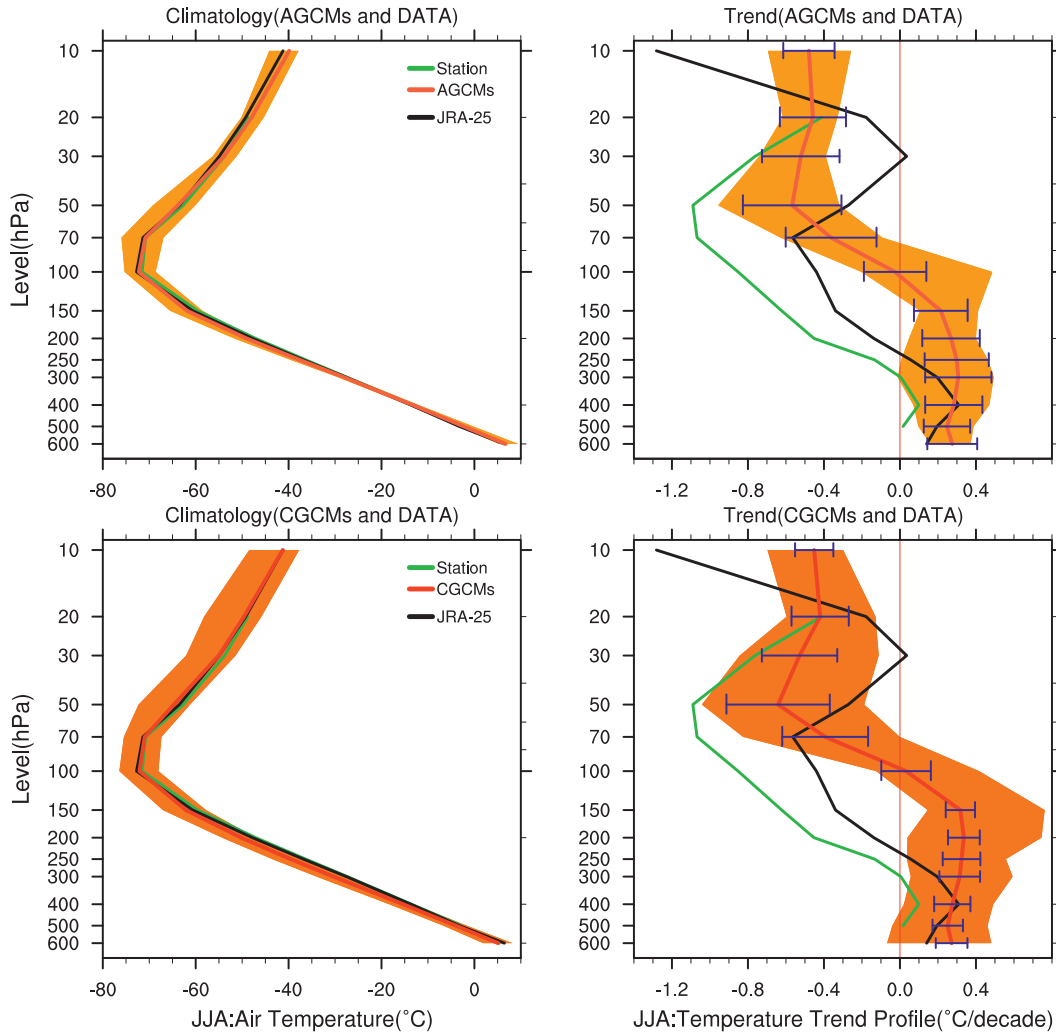


FIG. 11. (left) JJA mean temperature profile and (right) corresponding linear trends (blue bars represent the uncertainty with the 95% confidence intervals based on the standard error of the ensemble) over the TP during 1979–2005. The shading denotes the full range in models. The station observation is averaged by 14 radiosonde stations in JRA-25 and simulations; the temperature is interpolated to these radiosonde stations.

mean summer precipitation intensity, although the increased spatial resolution and inclusion of the sulfate aerosol indirect effects seems to improve the skill of the models to simulate the annual cycle of precipitation in both AGCMs and CGCMs. The interannual variability of the Tibetan high and the TPSM precipitation in most of the AGCMs closely resemble the historical observation due to the prescribed SST forcing field, while the observed seesaw pattern in the interannual variability of the TPSM and EASM can be reproduced by only a few models. Most of the GCMs successfully reproduced the tropospheric warming trend of recent decades and also the weakening trend in the surface heat low over the TP between 1979 and 2005, but the simulated warming amplitude was significantly larger than in the

observational data. Furthermore, the observed cooling trend in the upper troposphere and the decline of the Tibetan high were not simulated by most of the GCMs. In addition, although the observed meridional asymmetry in climate change over Eurasia (i.e., the larger warming amplitude in the mid- and high latitudes than in subtropics) and the resultant decelerated AWJ was reproduced by all AGCMs and most of the CGCMs, the trend was systematically weaker than the observations. Therefore, significant scope still exists for improving the simulation by GCMs of TPSM precipitation and regional climate change, especially in very mountainous areas.

Generally, the AGCMs performed better than the CGCMs in simulating the interannual variability and

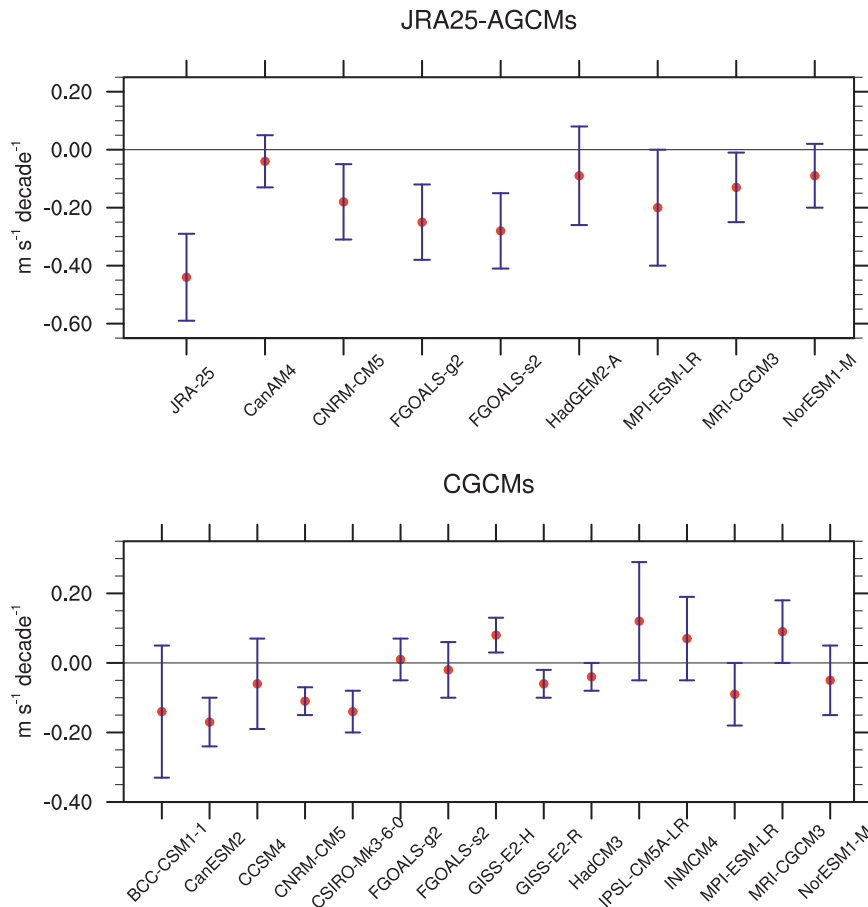


FIG. 12. The trend of the JJA mean 500-hPa AWJ index in JRA-25, 8 AGCMs, and 15 CGCMs during 1979–2005. Blue bars indicate the uncertainty (the 95% confidence intervals based on the standard error).

even the trend in the TPSM. This demonstrates the important role of the ocean in driving climate variability. The higher resolution of the models is expected to effectively improve the simulation skill, especially for the regional climate, but unfortunately, in this study, the advantage of a higher resolution was only reflected in a few aspects, such as the annual cycle of precipitation. This implies the critical role of the physical schemes in model performance. Forcing fields in the simulations including anthropogenic and natural forcings differ between models, suggesting that forcing differences explain some of the differences in temperature response between models. The dominating external influence is incoming solar radiation, but many aspects of the simulated climate also play an important role in modulating regional temperature and circulation, such as the cloud–radiation feedback and the complicated interactions between the atmosphere and the underlying land, ocean, snow, ice, and biosphere. In this paper, the indirect effects of sulfate aerosol were studied, although other

forcing factors, such as stratospheric chemistry, may also be considered in the future.

Climate variability ranges over very broad temporal and spatial scales, and the intrinsic linkages between them are not fully understood. Therefore, identifying the nature and extent of the interactions among these multiscale variations is imperative if we are to better understand climate change on our planet and develop the concepts necessary for ongoing model development.

Acknowledgments. We thank the two anonymous reviewers for constructive comments that were helpful for improving the overall quality of the paper. This work was jointly supported by the Strategic Priority Research Program–Climate Change: Carbon Budget and Related Issues of the Chinese Academy of Sciences (Grant XDA-05110303), the Chinese Ministry of Science and Technology (Grant 2010CB951703), and the National Natural Science Foundation of China (Grants 41175070 and 41275095).

REFERENCES

- Adler, R. F., and Coauthors, 2003: The Version-2 Global Precipitation Climatology Project (GPCP) monthly precipitation analysis (1979–present). *J. Hydrometeor.*, **4**, 1147–1167.
- Annamalai, H., K. Hamilton, and K. R. Sperber, 2007: The South Asian summer monsoon and its relationship with ENSO in the IPCC AR4 simulations. *J. Climate*, **20**, 1071–1092.
- Dee, D. P., and Coauthors, 2011: The ERA-Interim Reanalysis: Configuration and performance of the data assimilation system. *Quart. J. Roy. Meteor. Soc.*, **137**, 553–597.
- Duan, A. M., and G. X. Wu, 2005: Role of the Tibetan Plateau thermal forcing in the summer climate patterns over subtropical Asia. *Climate Dyn.*, **24**, 793–807.
- , and —, 2008: Weakening trend in the atmospheric heat source over the Tibetan Plateau during recent decades. Part I: Observations. *J. Climate*, **21**, 3149–3164.
- , and —, 2009: Weakening trend in the atmospheric heat source over the Tibetan Plateau during recent decades. Part II: Connection with climate warming. *J. Climate*, **22**, 4197–4212.
- , Y. M. Liu, and G. X. Wu, 2005: Heating status of the Tibetan Plateau from April to June and rainfall and atmospheric circulation anomaly over East Asia in midsummer. *Sci. China*, **48**, 250–257.
- , G. X. Wu, Q. Zhang, and Y. M. Liu, 2006: New proofs of the recent climate warming over the Tibetan Plateau as a result of the increasing greenhouse gases emissions. *Chin. Sci. Bull.*, **51**, 1396–1400.
- Duan, K. Q., T. D. Yao, N. L. Wang, L. D. Tian, and B. Q. Xu, 2008: Difference in precipitation variability between the north and south Tibetan Plateaus. *J. Glaciol. Geocryol.*, **30**, 726–732.
- Ebert, E. E., and J. L. McBride, 2000: Verification of precipitation in weather systems: Determination of systematic errors. *J. Hydrol.*, **239**, 179–202.
- Gao, X. J., J. S. Pal, and F. Giorgi, 2006: Projected changes in mean and extreme precipitation over the Mediterranean region from a high resolution double nested RCM simulation. *Geophys. Res. Lett.*, **33**, L03706, doi:10.1029/2005GL024954.
- Goswami, B. N., 1998: Interannual variations of Indian summer monsoon in a GCM: External conditions versus internal feedbacks. *J. Climate*, **11**, 501–522.
- Guo, L., E. J. Highwood, L. C. Shaffrey, and A. G. Turner, 2012: The effect of regional changes in anthropogenic aerosols on rainfall of the East Asian summer monsoon. *Atmos. Chem. Phys. Discuss.*, **12**, 23 007–23 038, doi:10.5194/acpd-12-23007-2012.
- Guo, Q., 1983: The summer monsoon intensity index in East Asia and its variation (in Chinese). *Acta Geogr. Sin.*, **38**, 207–217.
- Kalnay, E., and Coauthors, 1996: The NCEP/NCAR 40-Year Reanalysis Project. *Bull. Amer. Meteor. Soc.*, **77**, 437–471.
- Kanamitsu, M., W. Ebisuzaki, J. Woollen, S.-K. Yang, J. J. Hnilo, M. Fiorino, and G. L. Potter, 2002: NCEP–DOE AMIP-II Reanalysis (R-2). *Bull. Amer. Meteor. Soc.*, **83**, 1631–1643.
- Kang, I. S., and Coauthors, 2002: Intercomparison of the climatological variations of Asian summer monsoon precipitation simulated by 10 GCMs. *Climate Dyn.*, **19**, 383–395.
- Kusunoki, S., J. Yoshemura, H. Yoshimura, A. Noda, K. Oouchi, and R. Mizuta, 2006: Change of baiu rain band in global warming projection by an atmospheric general circulation model with a 20-km grid size. *J. Meteor. Soc. Japan*, **84**, 581–611.
- Lambert, S. J., and G. J. Boer, 2001: CMIP1 evaluation and intercomparison of coupled climate models. *Climate Dyn.*, **17**, 83–106.
- Lau, K.-M., K.-M. Kim, and S. Yang, 2000: Dynamical and boundary forcing characteristics of regional components of the Asian summer monsoon. *J. Climate*, **13**, 2461–2482.
- , S. C. Tsay, C. Hsu, and M. Chin, 2008: The Joint Aerosol–Monsoon Experiment: A new challenge for monsoon climate research. *Bull. Amer. Meteor. Soc.*, **89**, 369–383.
- Liu, X., 1998: Influences of Qinghai–Xizang (Tibet) Plateau uplift on the atmospheric circulation, global climate and environment changes (in Chinese). *Plateau Meteor.*, **18**, 321–331.
- Mason, R. B., and C. E. Anderson, 1963: The development and decay of the 100-mb. summertime anticyclone over southern Asia. *Mon. Wea. Rev.*, **91**, 3–12.
- Onogi, K., and Coauthors, 2007: The JRA-25 Reanalysis. *J. Meteor. Soc. Japan*, **85**, 369–432.
- Qian, Y., and F. Giorgi, 1999: Interactive coupling of regional climate and sulfate aerosol models over eastern Asia. *J. Geophys. Res.*, **104** (D6), 6477–6499.
- Rajendran, K., A. Kitoh, and S. Yukimoto, 2004: South and East Asian summer monsoon climate and variation in the MRI coupled model (MRI-CGCM2). *J. Climate*, **17**, 763–782.
- Sheng, C. Y., 1986: Main characteristics of Asian circulation. *An Introduction to the Climate of China* (in Chinese). Science Press, 85–89.
- Solomon, S., D. Qin, M. Manning, Z. Chen, M. Marquis, K. Averyt, M. Tignor, and H. L. Miller Jr., Eds., 2007: *Climate Change 2007: The Physical Science Basis*. Cambridge University Press, 996 pp.
- Tang, M. C., 1995: Discussion on interdecadal oscillation of the plateau monsoon and its cause. *Sci. Meteor. Sin.*, **15**, 64–68.
- , and E. R. Reiter, 1984: Plateau monsoons of the Northern Hemisphere: A comparison between North America and Tibet. *Mon. Wea. Rev.*, **112**, 617–637.
- , Z. Shen, and Y. Chen, 1979: On climate characteristics of the Xizang Plateau monsoon. *Acta Geogr. Sin.*, **34**, 33–42.
- Taylor, K. E., 2001: Summarizing multiple aspects of model performance in a single diagram. *J. Geophys. Res.*, **106** (D7), 7183–7192.
- Wang, B., 2006: *The Asian Monsoon*. Springer, 787 pp.
- , and LinHo, 2002: Rainy season of the Asian–Pacific summer monsoon. *J. Climate*, **15**, 386–398.
- , and Q. Ding, 2008: Global monsoon: Dominant mode of annual variation in the tropics. *Dyn. Atmos. Oceans*, **44**, 165–183.
- , I. S. Kang, and J. Y. Lee, 2004: Ensemble simulations of Asian–Australian monsoon variability by 11 AGCMs. *J. Climate*, **17**, 803–818.
- Webster, P. J., V. O. Magana, T. N. Palmer, J. Shukla, R. A. Tomas, M. Yanai, and T. Yasunari, 1998: Monsoons: Processes, predictability, and the prospects for prediction. *J. Geophys. Res.*, **103** (C7), 14 451–14 510.
- Wu, G. X., Y. M. Liu, B. He, Q. Bao, A. M. Duan, and F. F. Jin, 2012: Thermal controls on the Asian summer monsoon. *Sci. Rep.*, **2**, doi:10.1038/srep00404.
- Xu, Q., 2001: Abrupt change of the mid-summer climate in central east China by the influence of atmospheric pollution. *Atmos. Environ.*, **35**, 5029–5040.
- Ye, B., D. Yang, Y. Ding, T. Han, and T. Koike, 2004: A bias-corrected precipitation climatology for China. *J. Hydrometeor.*, **5**, 1147–1160.

- Yeh, D., and Y. Gao, 1979: *Meteorology of the Tibetan Plateau* (in Chinese). Science Publication Agency, 278 pp.
- , S. Tao, and M. Li, 1958: The abrupt change of the atmospheric circulation in June and October (in Chinese). *Acta Meteor. Sin.*, **29**, 249–263.
- Zeng, X. B., and E. Lu, 2004: Globally unified monsoon onset and retreat indexes. *J. Climate*, **17**, 2241–2248.
- Zhang, Q., Y. F. Qian, and X. H. Zhang, 2000: Interannual and interdecadal variations of the South Asia high (in Chinese). *Chin. J. Atmos. Sci.*, **24**, 67–78.
- Zhang, Q. Y., S. Y. Tao, and S. L. Zhang, 2003: The persistent heavy rainfall over the Yangtze River valley and its association with the circulations over East Asia during summer (in Chinese). *Chin. J. Atmos. Sci.*, **27**, 1018–1030.
- Zhao, P., S. Yang, and R. C. Yu, 2010: Long-term changes in rainfall over eastern China and large-scale atmospheric circulation associated with recent global warming. *J. Climate*, **23**, 1544–1562.
- Zhou, T. J., and R. C. Yu, 2006: Twentieth-century surface air temperature over China and the globe simulated by coupled climate models. *J. Climate*, **19**, 5843–5858.